Nonlinearity and Domain Switching in a 3D-Printed Architected Ferroelectric

Abhijit Pramanick,* Chaimae Babori, Frédéric Albertini, Frederik Holm Gjørup, Aurore Brézard Oudot, Ashutosh Kumar, Mads Ry Vogel Jørgensen, and Laurent Daniel

Recent advances in 3D printing have enabled fabrication of architected functional ceramics with tunable functionalities at reduced weight and cost. An essential cornerstone of materials design is to determine structure–property relations. For polycrystalline ferroelectrics, such relationships can be complex due to several microscopic mechanisms, such as lattice strains and/or domain switching, which show nonlinear dependence on external stimuli and are furthermore dependent on grain orientations. For architected materials, these microscopic mechanisms can also be spatially nonuniform. Herein, the development of appropriate methodology is entailed to correlate functional properties of architected ferroelectrics with spatial- and orientation-resolved microscopic mechanisms. Herein, using in situ orientation-resolved X-ray microdiffraction, it is shown that nonlinear polarization and strain responses in a 3D-printed architected ferroelectric are driven by localized progression of non-180° domain switching, which depends not only on the internal distribution of electric-field lines but also on the evolving long-range stress fields resulting from inhomogeneous domain-switching transformation strains. In this current study, it is indicated that nonlinear behavior in architected ferroelectrics can be effectively tuned by appropriate design of sample geometry, which controls the internal electric-field distribution in the material.

1. Introduction

Additive manufacturing (AM) refers to the process of fabricating 3D material components layer-by-layer based on a stack of digital 2D design files.[1–5] This approach has brought a paradigm shift in the manufacturing industry toward greater customization, speed, and functionality, whereby also lowering costs and materials waste.[6–9] Already, there is a growing demand for additively manufactured components in various industries, including automotive, aerospace, defense, biomedical, electronics, and renewable energy transition.[10–12] In addition to processing flexibility, AM has also opened a novel way for improving or enabling new functionalities by creatively arranging a combination of different materials and open spaces within a single component. Materials created in this manner are called "architected materials", which have proved to be disruptive in several technological areas.[1,6–9]

Over the last decade, 3D-printing technologies for AM of metal and polymer

A. Pramanick, C. Babori, A. B. Oudot, L. Daniel
Université Paris-Saclay
CentraleSupélec
CNRS
Laboratoire de Génie
Électrique et Électronique de Paris
91192 Gif-sur-Yvette, France
E-mail: abhijit.pramanick@centralesupelec.fr

A. Pramanick, C. Babori, L. Daniel
Sorbonne Universite
CNRS
Laboratoire de Genie Electrique et Electronique de Paris
75252 Paris, France

The ORCID identification number(s) for the author(s) of this article can be found under https://doi.org/10.1002/adem.202402104.

F. Albertini
Université Paris-Saclay
Université de Versailles Saint-Quentin-en-Yvelines
LISV
78124 Vélizy -Villacoublay, France

F. H. Gjørup, M. R. V. Jørgensen
Department of Chemistry & iNANO
Aarhus University
8000 Aarhus C, Denmark

F. H. Gjørup, M. R. V. Jørgensen
MAX IV Laboratory
Lund University
SE-221 00 Lund, Sweden

A. Kumar
Institut de Chimie Moléculaire et des Matériaux d'Orsay
University Paris-Saclay
91400 Orsay, France

A. Kumar
Department of Materials Science and Metallurgical Engineering
Indian Institute of Technology Bhilai
Chhattisgarh 491001, India

ADVANCED
SCIENCE NEWS

www.advancedsciencenews.com

ADVANCED
ENGINEERING
MATERIALS

www.aem-journal.com

parts have reached a certain level of maturity.[13] In comparison, 3D-printing technologies for ceramic components is still in its early stages.[2–4,14,15] Nevertheless, 3D printing of ceramics is attractive due to 1) demand for small-batch customized components, 2) difficulty in intricate machining due to inherent brittleness, and 3) desire to reduce waste owing to more expensive raw materials. Consequently, various technologies have been recently developed for AM of ceramic parts.[5,15] Notably, digital light processing (DLP) has gained significant popularity, in which a green body of ceramic–polymer composite is printed from a slurry of ceramic powders and organic additives fixated by localized light-induced photopolymerization.[16] Although, the market for 3D-printed ceramics is poised to grow tremendously, a prerequisite for the widespread adoption of 3D-printed ceramic parts is to improve their predictability in terms of performance and service life. This requires examination of the evolution of microscopic structural changes at grain, domain, and atomic scales. For 3D-printed architected materials, such relations should also encompass the effects of the topology of a component on heterogeneous structural evolution. Unfortunately, while the last few years saw tremendous progress in printing technologies and finite-element modeling of 3D-printed parts,[6,17,18] there is a lack of experimental studies on structure–property relationships from a traditional materials science perspective.

Ferroelectric ceramics are used in varied applications, including electromechanical actuators, load and heat sensors, telecommunications, electronics, solid-state cooling, and energy harvesting.[19] Some recent studies indicated that architected ferroelectrics may provide some unique advantages in comparison to monolithic ceramics.[20–24] However, the design of architected ferroelectrics based on linear constitutive relations alone, such as refs. [20–24], may not be sufficient since they do not account for commonly observed nonlinear behavior, which arise from field-dependent stochastic microstructural mechanisms, such as domain switching, phase transitions, or intergranular interactions.[25–31] Although non-180° domain switching is known to play a decisive role in macroscopic functional response of ferroelectrics,[25,28] no studies exist yet for spatial/orientation-resolved characterization of non-180° domain switching in 3D-printed architected ferroelectrics. Here, we used a novel experimental approach of 2-D micro-X-ray diffraction under applied electric fields to characterize the evolution of spatially inhomogeneous non-180° domain switching within an additively manufactured architected ferroelectric ceramic. We show that the progression of non-180° domain switching depends not only on the distribution of electric-field lines but is also strongly influenced by internal stress fields generated as a result of transformation strain from localized domain switching at regions with high field concentrations. Our results highlight the role of sharp geometric features in driving large localized structural changes in architected ferroelectrics, and how it influences macroscopic nonlinear dielectric and electromechanical behavior. The current study emphasizes the need to incorporate such information for better design of 3D-printed ferroelectric ceramics.

2. Results and Discussion

We fabricated 3D-printed $BaTiO_3$ ceramic plate samples in the form of a honeycomb-like structure with two interconnected hexagons, as shown in **Figure 1**a, using a combination of DLP and conventional solid-state synthesis, as further described in Experimental Section. A plate geometry was used to facilitate in situ characterization of the architected ceramic using X-rays in transmission geometry (vide infra). Among the different geometries for 2D lattice structures, the honeycomb structure was chosen since it is widely implemented due to its optimum combination of lighter weight, excellent load support, and mechanical stability.[32–34] In addition, we chose a Pb-free ferroelectric due to potential concerns about toxicity of Pb-based ferroelectrics that are widely used in the industry at present.[35] Among the Pb-free ferroelectrics, $BaTiO_3$ and its solid solutions have shown great promise for use in capacitors, sensors, and actuators,[36] and hence this material was chosen for the present study.

Figure 1b,c shows induced charge and surface displacement, respectively, for the architected ceramic under large cyclic voltage applied across the top and bottom plate electrodes. We used charge and voltage to represent the dielectric response, and displacement and voltage to represent the electromechanical response, since polarization, strain, and electric field are nonuniform across the architected material. Nonlinear dielectric behavior is characterized from the measured charge–voltage hysteresis loops under application of electric voltage cycles of increasing amplitudes. The pseudo-dielectric constant (not a true material constant) is obtained from the relation as follows

$$K = \frac{\text{Polarization}}{\text{Nominal Electric Field}} = \frac{\text{Charge per unit area}}{\text{Voltage/height}}$$
$$= p_{max} \times h / (2 \times V_0 \times A) \tag{1}$$

where K is the dielectric constant, A is the area of the top electrode, and h is the vertical height of the architected material, and all other variables are defined in Figure 1d. The pseudo converse piezoelectric constant (not a true material constant) is obtained from the relation as follows

$$d* = \frac{\text{Strain}}{\text{Nominal Electric Field}} = \frac{\text{Displacement/Height}}{\text{Voltage/Height}} = s_{max} / (V_0) \tag{2}$$

where $d*$ is the piezoelectric constant and all other variables are defined in Figure 1e. $d*$ is evaluated for both positive and negative applied electric fields, and averaged values are shown here. Figure 1f shows dielectric and piezoelectric constants as a function of nominal electric field, which is defined as V_0/h. The error bars provide the estimated standard deviations based on measurements over multiple electric-field cycles for the same applied voltage. There is a rapid increase in the dielectric and piezoelectric constants in the nominal electric-field range from 500 to 1000 V mm^{-1}, which exemplifies the regime with largest nonlinear behavior for the architected ferroelectric ceramic.

The measured polarization and strain hysteresis loops for the architected $BaTiO_3$ ceramics are different from what is typically observed for corresponding bulk monolithic ceramics, such as
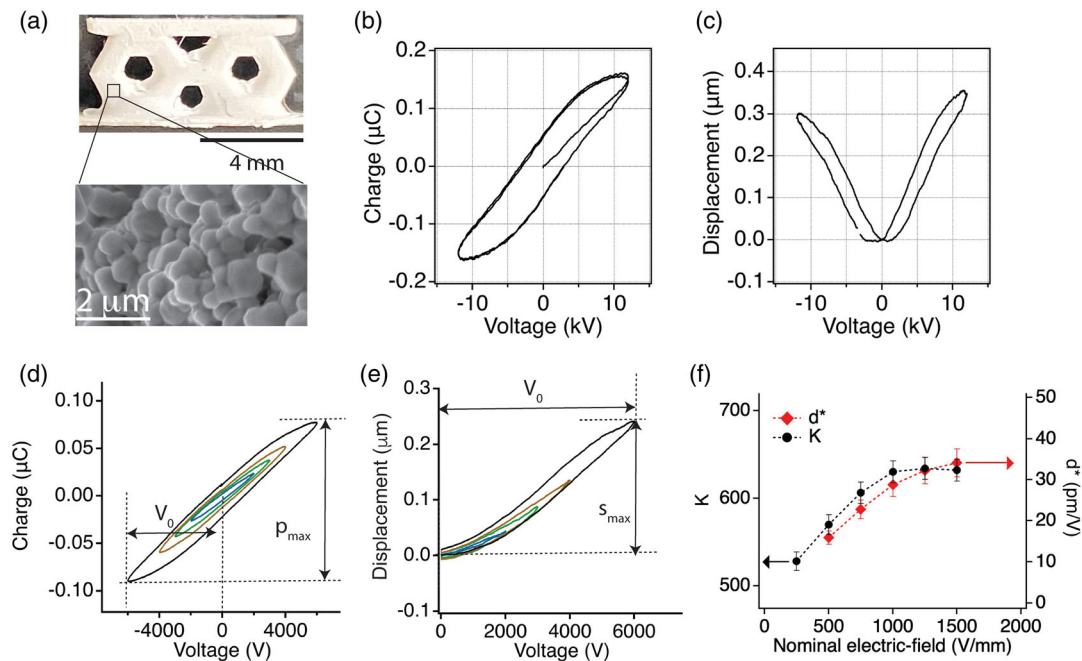
Figure 1. Fabrication and electrical characterization of a 3D-printed architected ferroelectric ceramic: a) a 3D-printed architected $BaTiO_3$ ceramic and SEM micrograph of its grain structure. b) Dielectric and c) electromechanical responses under application of large cyclic voltage across top and bottom plates of the architected ceramic. d) Dielectric and e) electromechanical responses of the architected ferroelectric under multiple electric-voltage cycles with different amplitudes, V_0. f) Pseudo-dielectric (K) and piezoelectric ($d*$) constants as function of nominal electric-field amplitude. The lines are used as guide for the eyes.

ref. [37]. For example, saturation polarization and strain values are not reached for the architected ceramics even under a high electric field amplitude of $3\,kV\,mm^{-1}$, while saturation is typically obtained for monolithic $BaTiO_3$ ceramics under electric field amplitudes of ≈ 1–$1.5\,kV\,mm^{-1}$.[37] The microscopic origin for the different macroscopic response in the architected ceramics is investigated with in situ diffraction experiments, as further described later. Additionally, the hysteresis loops for the architected $BaTiO_3$ ceramics also appear to be lossy under large electric field amplitude of $3\,kV\,mm^{-1}$, which could be due to the presence of residual photoresist materials on the surface of the grains in the 3D-printed ceramics.

In bulk ferroelectric ceramics, nonlinear functional response is mainly ascribed to domain-switching process.[25–31] However, unlike bulk ceramics, the electric field is not homogeneous across the entire volume of an architected ceramic. This is illustrated in **Figure 2**, which shows results from COMSOL modeling of the electric-field lines for this particular geometry. Note that simulations for two different geometries are shown: one is for the ideal design and the other geometry considers maximum deviation of the fabricated samples from the ideal design. In both cases, there is a concentration of electric field lines near some of the sharp corners, as indicated in the color maps and vector maps. This means that the domain-switching and other microscopic processes are expected to progress nonuniformly across the architected material. To investigate the effect of nonhomogeneous electric-field distribution on the macroscopic nonlinear behavior of an architected ferroelectric, we undertook direct structural characterization using in situ 2D

microdiffraction. The microdiffraction experiment was conducted at the DanMAX beamline at the MAX IV laboratory. **Figure 3**a shows the experimental setup. The measured 2D diffraction rings were segmented into different azimuthal orientations to probe the structural changes along different directions with respect to the vertical electric-field direction (Figure 3b). Note that, here, we do not distinguish between the structural changes in two directions that are misoriented by 180°, which is a good approximation for non-180° domain switching and lattice strains processes.[28] Figure 3c shows an exemplary {200} diffraction peak profile measured for one beam position and for the 90° azimuthal segment (along the vertical direction). The {200} peaks were fitted with two asymmetric peak profile functions to account for 002 and 200 plane normals from two sets of 90° domain variants. The asymmetric nature of the peaks accounts for lattice strains introduced near 90° domain boundaries.[38] The top panel of Figure 3d shows map for $\rho = I(002) - I(200)$, where I refers to the integrated intensities of the 002 and 200 diffraction peaks. The bottom panel of Figure 3d shows map for the 2θ position of the 111 diffraction peak, which was obtained by fitting 111 peaks with a symmetric peak profile.

The progression of 90° domain switching within the architected material is shown by plotting the function $\Delta\rho = \rho_{V=0} - \rho_V$ for different magnitudes of applied electric voltages, V, as shown in **Figure 4**a. Figure 4b shows vector plots that indicate the magnitude and direction of the largest degree of non-180° domain switching at each position, which is obtained by comparing $\Delta\rho$ for different angular orientations. These plots
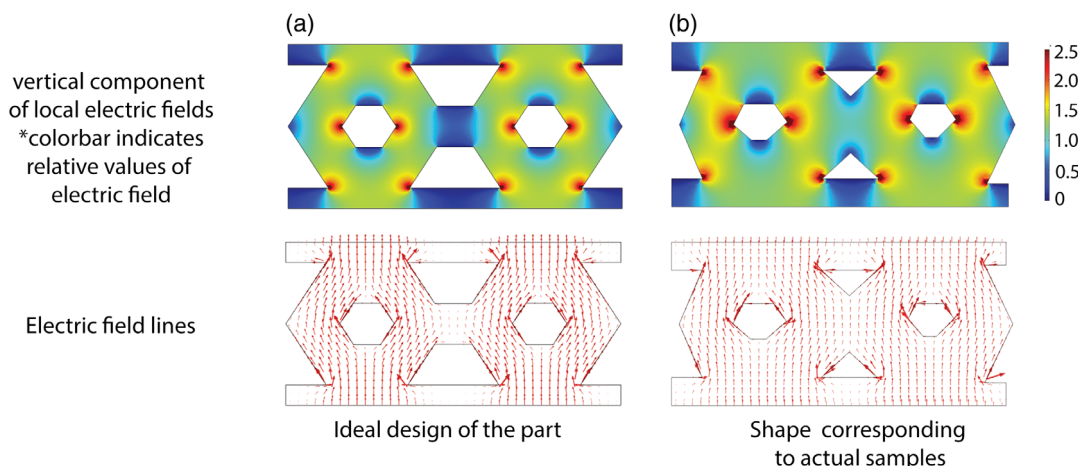
Figure 2. COMSOL simulation of the electric-field lines within the architected material with an electric-field applied across the top and bottom electrodes. The top panel shows the relative magnitude of the vertical component of the electric field, while the bottom panel shows the distribution of electric-field lines. The lengths of the arrows indicate the relative strength of the local electric fields. Two different geometries are considered: a) ideal design, and b) shape taking into account maximum deviation of the fabricated samples from the ideal design.

indicate a few remarkable aspects of the domain-switching process. First, significant 90° domain-switching commences in areas near the inside sharp corners, which roughly correspond to some of the regions with electric-field concentration, as indicated by COMSOL models. However, not all areas with higher field concentrations show the same degree of non-180° domain switching. This is likely because of the potential large depolarization fields near the internal free surfaces without electrodes, which makes it unfavorable for change in the existing domain structure.[39] Second, with increasing field, the areas with large degree of domain switching spread at a faster rate sideways between the two top corners of the hexagon. This is not entirely consistent with the COMSOL models since the electric-field lines are weaker in the region connecting the two top corners of the hexagon. Third, the largest degree of 90° domain switching within the two hexagonal arms is observed for the vertical direction, even though the COMSOL model indicates that the electric-field lines are oriented away from the vertical direction. These results, therefore, clearly indicate that the progression of 90° domain switching process within the architected material is influenced by factors other than only the distribution of the electric-field lines.

Next, for a detailed examination of the domain-switching process, we evaluated changes in the integrated diffraction patterns over a selected region, such as depicted in Figure 4a. For this region, Figure 4c shows relative changes in 002/200 peak for different applied voltages, for the $\omega = 90°$. The change in relative intensities of the 002/200 peaks reflects the change in volume fraction of 90° domains under the application of an electric voltage, as illustrated on the right panel of Figure 4c. For unpoled tetragonal ferroelectric, $I(002)/I(200)$ is ideally equal to the ratios of the reflection multiplicities $m(002)/m(200) = 0.5$, which is observed for all azimuthal sectors at $E = 0$. For higher fields, $I(002)/I(200)$ is increased for directions parallel to the electric field ($\omega = 90°$) and is decreased for directions perpendicular to the electric field ($\omega = 0°$), with continuous variations for

intermediate azimuthal angles (Figure 4d). These findings are consistent with earlier measurements of non-180° domain switching in monolithic ceramics.[28,40] For $\omega = 90°$, there is a rapid nonlinear increase in 90° domain switching over the boxed region for $V \geq 2000$, as indicated in the voltage dependence of $I(002)/I(200)$ (Figure 4e). The voltage range of ≈ 2000–3200 V, over which a nonlinear increase in $I(002)/I(200)$ is observed, is well correlated with the nominal electric-field range (voltage/height) over which the material also exhibits a linear increase in dielectric constant, K, and piezoelectric constant, $d*$ (Figure 1f). It is therefore clear that the macroscopic "apparent" dielectric and electromechanical nonlinearity is not the consequence of inhomogeneous field distribution alone, but instead directly related to local non-180° domain switching, which is a key to understanding the functional response of architected ferroelectric ceramics.

An interesting question is what causes the localized progression of non-180° domain switching, such as observed here for the particular geometry of a honeycomb-like structure. As shown earlier, non-180° domain switching in ferroelectric ceramics can be influenced by intergranular stresses,[28,40] which arise as a result of misfit strain between grains with large non-180° domain switching and surrounding matrix with lower/zero domain switching. For tetragonal crystals, the transformation strain from 90° domain switching is ideally zero along the $<111>$ directions, and hence, {111} lattice strains can be used as a gauge for the distribution of local intergranular stresses.[41] **Figure 5**a,b shows the corresponding vector maps indicating the magnitude and direction of the largest tensile and compressive {111} lattice strains, respectively. These maps were obtained from the measured changes in the (111) peak position with the applied electric field, such as depicted in Figure 5c. Clearly, the area with the largest degree of tensile {111} lattice strain corresponds to the same for non-180° domain switching. The areas with the largest degree of compressive {111} lattice strain are located above and below the region with the largest

**ADVANCED
SCIENCE NEWS**

www.advancedsciencenews.com

**ADVANCED
ENGINEERING
MATERIALS**

www.aem-journal.com
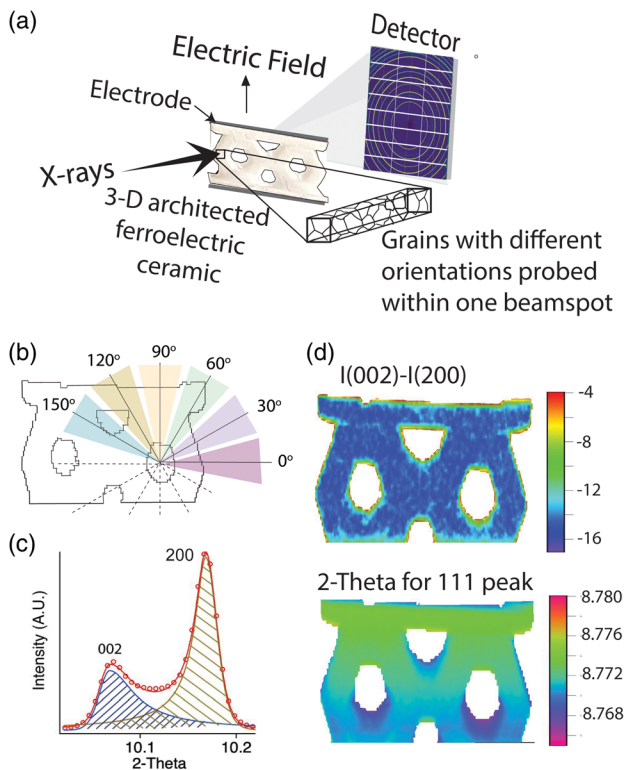
Figure 3. In situ structural characterization of 3D-printed architected ferroelectric ceramic: a) Experimental setup for in situ micro-X-Ray diffraction experiment from an architected material under an applied electric field. The experiment is performed in transmission geometry with an area detector. b) The Debye–Scherrer rings measured for each beam position are segmented into different azimuthal sectors as indicated. Note that, here, we do not distinguish between positive and negative directions of the same angular segment; that is, for example, 30° and 150° segments are not distinguished. c) Fitting of the 002/200 peaks is carried out, assuming a tetragonal crystal structure of the material. The relative change in volume fractions of the 90° domains is obtained from the integrated areas under the 002 and 200 peaks, as shown. d) Examples of maps containing structural information. The map on top shows the distribution of the quantity $\rho = I(002) - I(200)$, where I indicates the integrated peak areas. The map on the bottom shows the measured 2θ position of the 111 diffraction peak. The gradient in 2θ position is due to slight out-of-plane tilt of the sample; however, this has no influence on the intensity-dependent parameters and cancels out for the position-dependent parameters (strain).

domain switching. Further relation between {111} lattice strain and the 90° domain switching process is observed from the nonlinear voltage-dependent increase in the {111} lattice strain, as shown in Figure 5d. Indeed, the trend in Figure 5d is qualitatively similar to that for I(002)/I(200) ratio shown in Figure 4e, both of which are evaluated over the same rectangular boxed region. These results establish that the spatial distribution of {111} lattice strain in the architected ferroelectric is strongly correlated to the same for 90° domain switching. This insight can be used to understand the localized progression of non-180° switching, as described later.

Note that the COMSOL model indicates a sharp rise in the electric field near the various corners (Figure 2), which acts as initiation sites for localized domain switching. As 90° domain

switching commences at these regions, it introduces long-range stress fields. For the regions outlined by rectangular boxes in Figure 4a, the transformation strain from 90° domain switching causes them to expand in the vertical direction and shrink in the horizontal direction. This introduces long-range compressive and tensile stress fields in the surrounding matrix along the vertical and horizontal directions, respectively, as schematically illustrated in the top panel of Figure 5e. To evaluate this, we plot the {111} lattice strain distribution along line A–B as indicated in Figure 5a. Notably, as indicated by the {111} tensile lattice strain line profile, the internal tensile stress field extends asymmetrically outward and sideways from the point B. The line profile for the {111} lattice strain can further be fitted using a power law, indicating the long-range nature of the intergranular stresses introduced by localized domain switching. A similar line profile is observed for the I(002)/I(200) ratio but with steps that are contained within the envelope of the lattice strain profile. Considering that the {111} strain is entirely due to domain switching transformation strain, the long-range stress field can be estimated from Young's modulus of $BaTiO_3$, which is of the order of 5–10 MPa. This range of tensile stress is significant in further promoting 90° domain switching in $BaTiO_3$.[6] Therefore, based on these results, we propose that the long-range internal stress field caused by localized 90° switching promotes further progression of non-180° switching in certain directions that experience tensile stress while suppressing the same in other directions that experience compressive stress. This explains the anisotropic progression of the domain switching front in the architected material, as depicted in Figure 4.

3. Conclusion

In summary, we show that the nonlinear dielectric and electromechanical responses of an architected ferroelectric ceramic are driven by spatially localized progression of non-180° domain switching, which is different from that observed for monolithic bulk ceramics. The localized progression of domain switching in architected ceramics is caused by a convolution of two factors: 1) the distribution of electric-field lines and 2) the internal stress field introduced by misfit strains between different parts of the material under applied electric voltage. The former can be obtained by finite-element models. However, the latter aspect requires a deeper understanding of coupling between the different microscopic mechanisms, such as domain switching and intergranular stress. To this end, detailed examination of heterogeneous stimuli-induced microscopic processes remain to be explored in specific geometries of architected materials, which have shown promise in terms of both mechanical and functional properties such as described in refs. [1,6,42,43]. Advances in 3D-printing technologies for ceramic materials, such as presented in this article, constitute an essential step toward such undertakings. In addition, the experimental method of in situ 2D scanning X-Ray microdiffraction, as outlined here, provides a means to investigate the heterogeneous microscopic mechanisms in not only architected ferroelectrics but can also be expanded to other architected functional ceramics.
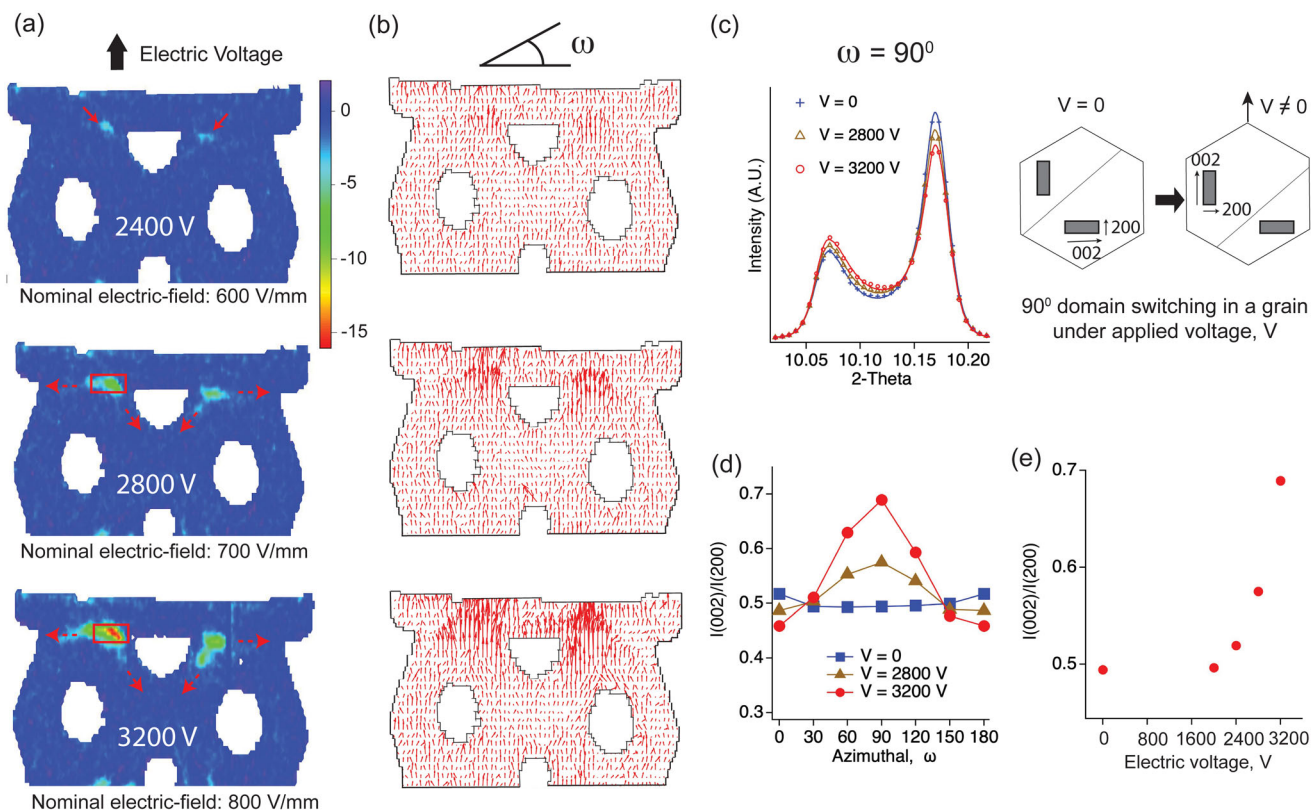
Figure 4. In situ measurement of spatial- and orientation-resolved electric-field-induced domain switching in architected ferroelectric ceramic: a) maps showing the intensity of structural change, namely, the quantity, $\Delta\rho = \rho_{V=0} - \rho_V$, where $\rho_V = I(002) - I(200)$ under applied electric voltage V. b) Vector maps showing the magnitude and direction of the largest electric-field-induced changes in different parts of the architected material. The largest values of $\Delta\rho$, or 90° domain switching, are observed near the top inside corners of the two hexagons and for the vertical direction. These maps indicate that the region with the largest electric-field-induced domain switching commences near the top inside corners of the hexagons and spreads sideways and outward as a function of the applied field. c) Peak profile of 002/200 peaks as a function of applied electric voltage for $\omega = 90°$ for the region indicated by the box in (a). Increase in relative intensity of 002 peak is caused by an increase in domain population with 002 plane normal parallel to the diffraction vector, as illustrated on the right. d) Orientation dependence of $I(002)/I(200)$ for different electric voltages for the region indicated by the box in (a). For the boxed region, $I(002)/I(200)$ is maximum for $\omega = 90°$ and minimum for $\omega = 0°$. The lines are used as guide for the eyes. e) Voltage dependence of $I(002)/I(200)$ for the azimuthal sector of $\omega = 90°$. There are unobservable changes below 2000 V, while above 2000 V, $I(002)/I(200)$ exhibits a nonlinear increase with the applied voltage.

4. Experimental Section

Fabrication of Architected Ceramics: The architected ceramic samples were prepared using a combination of DLP and conventional solid-state synthesis. The various steps for sample preparation are outlined in **Figure 6**a.

Fabrication of Architected Ceramics: Preparation of CAD Files: The digital files for 3D printing were generated using commercial CAD software—rhinoceros and grasshopper. A honeycomb-like structure was used for the preparation of test samples for electrical characterization and in situ structural characterization using X-Ray diffraction. A digital design file for a test sample in standard tesselation language (STL) format with two cells of a honeycomb structure was prepared, as shown in Figure 6b. The STL file was subsequently imported into Tethonware software by Tethon 3D, which slices the model and prepares the G-code for the printer.

Fabrication of Architected Ceramics: Preparation of Slurry for Printing: The preparation of the slurry for printing further consisted of two steps, as detailed in the following. 1) A powdered sample of ferroelectric barium titanate ($BaTiO_3$) was procured from a commercial supplier, Sigma Aldrich. The procured powder sample was first wet ground in a ball mill and subsequently dried to obtain powders with uniform and fine particle size in the range of $\approx 0.5-1$ μm size. 2) The $BaTiO_3$ powder was mixed with a photocurable polymer resin, Genesis Development Resin, supplied by Tethon 3D. ≈ 100 g of $BaTiO_3$ powder was used to prepare a batch of printing slurry and the volume fraction of the powder in the slurry was maintained at 20–25%. The powder was thoroughly dispersed within the polymer resin by vigorous stirring. For uniform dispersion of the powder particles, a few drops of a commercial paint thinner were also added to the mixture.

Fabrication of Architected Ceramics: Printing of Architected Samples: The layer-by-layer fabrication of the green body (ceramic and polymer composite) was undertaken using BISON 1000 3D printer supplied by Tethon 3D. The printer used was based on the DLP technique, in which the layer-by-layer synthesis was performed in a top-down approach. The slurry containing the powder sample and the photocurable resin was exposed to a continuous UV light emitting diode radiation with a wavelength of 405 nm. A digital mask was used to block part of the incident radiation so that the slurry was solidified only at selective locations. The spatial X/Y resolution for the printer was 57 μm. In the top-down approach, the first layer was printed on a base plate, and subsequent layers were then printed on the preceding layers as the base plate was pulled upward. The layer thickness for printing of each layer was maintained
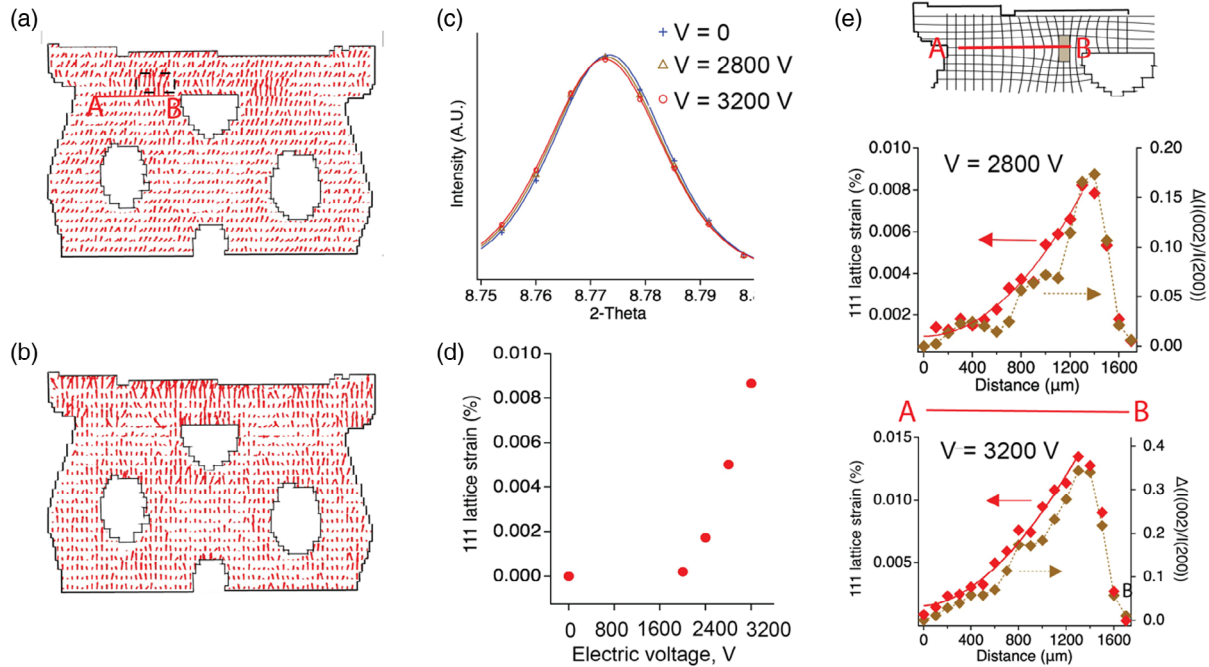
Figure 5. In situ measurement of tensile and compressive strain distributions in architected ferroelectric ceramic under electric field: a) vector map showing tensile {111} lattice strain for applied voltage of 2800 V. b) Same as (a), but for compressive {111} lattice strain. c) (111) peak profile as a function of applied voltage. The peaks shown are obtained from diffraction patterns integrated over the boxed region. d) {111} lattice strain obtained from fitting of the (111) diffraction peaks. The {111} lattice strain shows similar nonlinear voltage dependence with non-180° domain switching, indicating a major contribution from intergranular stress rather than the piezoelectric effect. e) Line profiles of {111} lattice strain and $I(002)/I(200)$ along the line A–B. The top schematically illustrates the long-range stress fields introduced due to transformation strain from localized non-180° domain switching within the architected material.
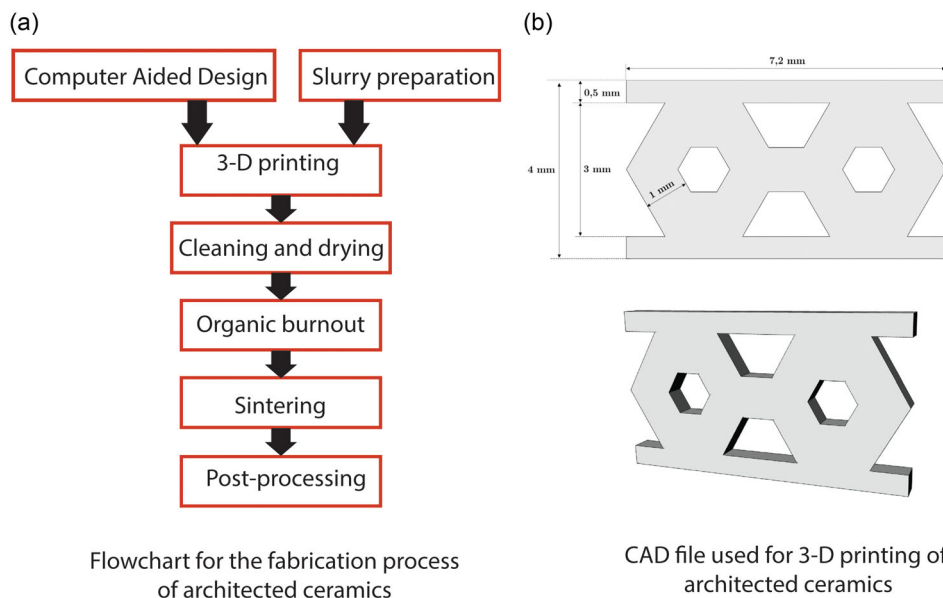
Figure 6. Design and fabrication steps of architected ceramics: a) flowchart showing steps for preparation of the architected ceramic in its final form. b) Dimensions for the STL file used for 3D printing.

at 50 μm. A relatively lower light intensity was used with longer exposure times, such as 380 s of exposure time per layer for first few layers and 180 s per layer after that. This translated to an incident energy of ≈900 mJ cm^{-2} for printing of the first ten layers and an incident energy of ≈450 mJ cm^{-2} for subsequent layers. The light intensity was adjusted to provide ideal combination of curing depth and resolution of the printed parts. The green

**ADVANCED
SCIENCE NEWS**

www.advancedsciencenews.com

**ADVANCED
ENGINEERING
MATERIALS**

www.aem-journal.com

body was extracted from the base plate after printing the entire sample. The residual slurry was cleaned from the printed sample first using a commercial cleaner and then running water.

Fabrication of Architected Ceramics: Sintering of the Green Bodies: Final ceramic samples were obtained from the printed green bodies after polymer burnout and sintering. These steps were undertaken carefully to avoid disintegration of the printed body, which can result from the development of gaseous products generated during the heat treatment due to high organic content. To alleviate this, the printed green bodies were first slowly heated in a tube furnace under an Ar atmosphere from room temperature to 550 °C with a heating rate of 60 °C h^{-1}, followed by a constant temperature plateau at 550 °C for 3 h. This procedure ensured that most of the polymer was burned out. The inert Ar atmosphere ensured that the organic content was first transformed into carbon without oxidation. In the second step, the samples were heated to a higher temperature of 1250 °C with a faster heating rate of 100 °C h^{-1}, followed by 16 h at a constant temperature of 1250 °C. The residual carbon generated due to the pyrolysis of the organic components during the first step was subsequently oxidized to CO_2 in this second step. The powder particles underwent sintering and grain growth at high temperatures to produce the final ceramic samples. Following sintering at high temperature, the samples were cooled down with a controlled cooling rate of 100 °C h^{-1} to 500 °C, after which the furnace was cooled down to room temperature. Figure 1a shows an exemplary architected ceramic sample. The microstructure of the architected ceramics was characterized using a Thermo Scientific Phenom XL G2 Desktop scanning electron microscope (SEM). Figure 1a shows the dense microstructure of the sintered ceramic sample with grain sizes on the order of a few micrometers.

In total, four samples with optimal processing conditions were prepared for electrical characterization and structural characterization using in situ X-Ray diffraction.

Fabrication of Architected Ceramics: Electrical Characterization of Architected Ceramics: We measured the electric-field-induced polarization and induced strain in the architected ceramic using the same experimental setup described in ref. [44]. The procedure, including illustrations and explanations with figures, is included in that work. The procedure involved placing the sample between two fixtures, electrically insulating it with Teflon pieces, and immersing it in a polytetrafluoroethylene container filled with insulating oil to prevent dielectric breakdown. A low-rigidity spring ensured contact with the upper electrode while minimizing the stresses induced by the spring. The electric field was generated by a high-voltage amplifier (Trek 20/20 C-HS) and controlled by a dSPACE hardware module in real time with a maximum sampling rate of 5 kHz. Dielectric displacement was measured from the top electrode using an operational amplifier integrator circuit, and the measurements were recorded via the dSPACE hardware module. The sample elongation L3 was measured using the CCD laser sensor LK-G10 connected to a LK-GD500 controller from Keyence.

Fabrication of Architected Ceramics: In Situ 2D X-Ray Microdiffraction of Architected Ceramics: The structural characterization of the architected $BaTiO_3$ ceramic samples was undertaken at the DanMAX beamline at the MAX IV laboratory. A 35.000 keV X-Ray beam was focused to 82×70 μm ($h \times v$, full width at half maximum). The diffracted X-rays were detected using a DECTRIS PILATUS3 X 2M CdTe area detector. The sample to detector was 630 mm. The detector geometry was calibrated using the pyFAI software on data collected on an LaB6 standard reference material from NIST (SRM 660c).[45] The samples were mounted on a 3D-printed sample holder incorporating the two high voltage electrodes. The sample holder was mounted on a set of XY stages to raster scan the sample through the X-Ray beam. A continuous scanning scheme is used to speed up the data acquisition. Here, each vertical line is scanned in one continuous motion at constant velocity while the detector is electronically triggered at a specified frequency. The samples were scanned with a resolution of 50 μm in both horizontal and vertical directions. Each diffraction image was collected for 20 ms, i.e., a frame rate of 50 Hz. The raw data was azimuthally integrated using specified azimuthal bins using a Python version of the (matrix multiplication facilitated radial and azimuthal integration algorithm) algorithm.[46]

Conflict of Interest

The authors declare no conflict of interest.

Author Contributions

Abhijit Pramanick: conceptualization: (equal); data curation: (equal); formal analysis: (equal); funding acquisition: (equal); investigation: (lead); methodology: (lead); project administration: (equal); visualization: (lead); writing—original draft: (lead); writing—review & editing: (lead). **Chaimae Babori**: data curation: (equal); formal analysis: (supporting); investigation: (supporting); writing—review & editing: (equal). **Frédéric Albertini**: data curation: (equal); formal analysis: (supporting); investigation: (equal); writing—review & editing: (equal). **Frederik Holm Gjørup**: data curation: (equal); formal analysis: (equal); software: (equal); writing—review & editing: (equal). **Aurore Brézard Oudot**: data curation: (equal); investigation: (equal). **Ashutosh Kumar**: data curation: (equal); methodology: (equal); writing—review & editing: (equal). **Mads Ry Vogel Jørgensen**: data curation: (equal); investigation: (equal); methodology: (equal); software: (equal); writing—review & editing: (equal). **Laurent Daniel**: conceptualization: (equal); data curation: (equal); funding acquisition: (equal); investigation: (equal); project administration: (equal); validation: (equal); writing—review & editing: (equal).

Data Availability Statement

The data that support the findings of this study are available from the corresponding author upon reasonable request.

[1] X. Xia, C. M. Spadaccini, J. R. Greer, *Nat. Rev. Mater.* **2022**, *7*, 683.
[2] H. Cui, R. Hensleigh, H. Chen, X. Zheng, *J. Mater. Res.* **2018**, *33*, 360.
[3] Z. Chen, Z. Li, J. Li, C. Liu, C. Lao, Y. Fu, C. Liu, Y. Li, P. Wang, Y. He, *J. Eur. Ceram. Soc.* **2019**, *39*, 661.

[4] R. P. Chaudhary, C. Parameswaran, M. Idrees, A. S. Rosaki, C. Liu, Z. Chen, P. Colombo, *Prog. Mater. Sci.* **2022**, *128*, 100969.

[5] Z. C. Eckel, C. Zhou, J. H. Martin, A. J. Jacobsen, W. B. Carter, T. A. Schaedler, *Science* **2016**, *351*, 58.

[6] N. A. Fleck, V. S. Deshpande, M. F. Ashby, *Proc. R. Soc. A* **2010**, *466*, 2495.

[7] L. Montemayor, V. Chernow, J. R. Greer, *MRS Bull.* **2015**, *40*, 1122.

[8] I. Gibson, D. Rosen, B. Stucker, in *Additive Manufacturing Technologies: 3D Printing, Rapid Prototyping and Direct Digital Manufacturing*, 2nd edition, Springer, New York **2015**.

[9] F. Wang, M. Brøns, O. Sigmund, *Adv. Funct. Mater.* **2023**, *33*, 2211561.

[10] S. A. M. Tofail, E. P. Koumoulos, A. Bandyopadhyay, S. Bose, L. O'Donoghue, C. Charitidis, *Mater. Today* **2018**, *21*, 22.

[11] C. L. Ventola, *Medical Applications for 3D Printing: Current and Projected Uses, P&T* **2014**, *39*, 704.

[12] R. Hensleigh, H. Cui, Z. Xu, J. Massman, D. Yo, J. Berrigan, X. Zheng, *Nat. Electron.* **2020**, *3*, 216.

[13] A. Aversa, A. Saboori, G. Marchese, L. Luliano, M. Lombardi, P. Fino, *J. Mater. Eng. Perform.* **2021**, *30*, 8689.

[14] M. Dadkhah, J.-M. Tulliani, A. Saboori, L. Iuliano, *J. Eur. Ceram. Soc.* **2023**, *43*, 6635.

[15] J. Deckers, J. Vleugels, J.-P. Kruth, *J. Ceram. Sci. Technol.* **2014**, *5*, 245.

[16] O. Santoliquido, P. Colombo, A. Ortona, *J. Eur. Ceram. Soc.* **2019**, *39*, 2140.

[17] J. C. Sänger, B. R. Pauw, B. Riechers, A. Zocca, J. Rosalie, R. Maaß, H. Sturm, J. Günster, *Adv. Mater.* **2023**, *35*, 2208653.

[18] Y. Xu, Y. Gao, X. Yang, C. Tian, Z. Yang, J. Zhang, *J. Eur. Ceram. Soc.* **2023**, *43*, 4263.

[19] K. Uchino, in *Ferroelectric Devices*, Marcel Dekker, New York, NY **2000**.

[20] S. Iyer, M. Alkhader, T. A. Venkatesh, *Int. J. Solids Struct.* **2016**, *80*, 73.

[21] K. S. Challagulla, T. A. Venkatesh, *Acta Mater.* **2012**, *60*, 2111.

[22] H. Cui, D. Yao, R. Hensleigh, H. Lu, A. Calderon, Z. Xu, S. Davaria, Z. Wang, P. Merceier, P. Tarazaga, X. Xheng, *Science* **2022**, *376*, 1287.

[23] H. Cui, R. Hensleigh, D. Yao, D. Maurya, P. Kumar, M. G. Kang, S. Priya, X. Zheng, *Nat. Mater.* **2019**, *18*, 234.

[24] J. Shi, K. Ju, H. Chen, A. Mirabolghasemi, S. Akhtar, A. Sasmito, A. Akbarzadeh, *Nano Energy* **2024**, *123*, 109385.

[25] D. Damjanovic, *J. Am. Ceram. Soc.* **2005**, *88*, 2663.

[26] E. K. H. Salje, *Annu. Rev. Mater. Res.* **2012**, *42*, 1.1.

[27] A. Pramanick, A. D. Prewitt, J. S. Forrester, J. L. Jones, *Crit. Rev. Solid State Mater. Sci.* **2012**, *37*, 243.

[28] A. Pramanick, D. Damjanovic, J. E. Daniels, J. C. Nino, J. L. Jones, *J. Am. Ceram. Soc.* **2011**, *94*, 293.

[29] H. Simons, A. B. Haugen, A. C. Jakobsen, S. Schmidt, F. Stöhr, M. Majkut, C. Detlefs, J. E. Daniels, D. Damjanovic, H. F. Poulsen, *Nat. Mater.* **2018**, *17*, 814.

[30] L. Daniel, D. A. Hall, J. Koruza, K. G. Webber, A. King, P. J. Withers, *J. App. Phys.* **2015**, *117*, 174104.

[31] F. Grigio, S. Jesse, A. Kumar, O. Ovchinnikov, H. Kim, T. N. Jackson, D. Damjanovic, S. V. Kalinin, S. Trolier-McKinstry, *Phys. Rev. Lett.* **2012**, *108*, 157604.

[32] H. N. G. Wadley, *Phil. Trans. Royal Soc. A* **2006**, *364*, 31.

[33] J. R. Greer, V. S. Deshpande, *MRS Bull.* **2019**, *44*, 750.

[34] D. J. McGregor, S. Tawfick, W. P. King, *Addit. Manuf.* **2018**, *25*, 10.

[35] A. J. Bell, O. Deubzer, *MRS Bulletin* **2018**, *43*, 581.

[36] M. Acosta, N. Novak, V. Rojas, S. Patel, R. Vaish, J. Koruza, G. A. Rossetti Jr., J. Rödel, *Appl. Phys. Rev.* **2017**, *4*, 041.305.

[37] V. Buscaglia, C. A. Randall, *J. Eur. Ceram. Soc.* **2020**, *40*, 3744.

[38] J. E. Daniels, J. L. Jones, T. R. Finlayson, *J. Phys. D: Appl. Phys.* **2006**, *39*, 5294.

[39] D. Zhao, T. Lenz, G. H. Gelinck, P. Groen, D. Damjanovic, D. M. de Leeuw, I. Katsouras,, *Nat. Commun.* **2019**, *10*, 2547.

[40] A. Pramanick, J. E. Daniels, J. L. Jones, *J. Am. Ceram. Soc.* **2009**, *92*, 2300.

[41] D. A. Hall, A. Steuwer, B. Cherdhirunkorn, T. Mori, P. J. Withers, *J. Appl. Phys.* **2004**, *96*, 4245.

[42] A. A. Zadpoor, M. J. Mirzaali, L. Valdevit, J. B. Hopkins, *APL Mater.* **2023**, *11*, 020401.

[43] X. Zhang, Y. Wang, B. Ding, X. Li, *Small* **2020**, *16*, 1902842.

[44] J. Kieffer, V. Valls, N. Blanc, C. Hennig, *J. Synchrotron Rad.* **2020**, *27*, 558.

[45] V. Segouin, M. Domenjoud, Y. Bernard, L. Daniel, *J. Eur. Ceram. Soc.* **2019**, *39*, 2091.

[46] A. B. Jensen, T. E. K. Christensen, C. Weninger, H. Birkedal, *J. Synchrotron Rad.* **2022**, *29*, 1420.